MNRAS 000, 1–14 (2020) Preprint 5 December 2021 Compiled using MNRAS LaTeX style file v3.0

New constraints on the 1.4 GHz source number counts and luminosity functions in the Lockman Hole field

Matteo Bonato[1,2⋆], Isabella Prandoni[3], Gianfranco De Zotti[2], Marisa Brienza[4,3], Raffaella Morganti[5,6] and Mattia Vaccari[7,8,3]

[1] *INAF−Istituto di Radioastronomia and Italian ALMA Regional Centre, Via Gobetti 101, I-40129, Bologna, Italy*
[2] *INAF−Osservatorio Astronomico di Padova, Vicolo dell'Osservatorio 5, I-35122, Padova, Italy*
[3] *INAF−Istituto di Radioastronomia, Via Gobetti 101, I-40129, Bologna, Italy*
[4] *Dipartimento di Fisica e Astronomia, Universitá di Bologna, via P. Gobetti 93/2, 40129, Bologna, Italy*
[5] *Kapteyn Astronomical Institute, University of Groningen, PO Box 800, 9700 AV, Groningen, The Netherlands*
[6] *ASTRON, Netherlands Institute for Radio Astronomy, Oude Hoogeveensedijk 4, 7991 PD, Dwingeloo, The Netherlands*
[7] *Department of Physics and Astronomy, University of the Western Cape, Private Bag X17, Bellville 7535, South Africa*
[8] *Inter-University Institute for Data Intensive Astronomy, South Africa*

arXiv:2010.08748v2 [astro-ph.GA] 5 Dec 2020

Released 2020 Xxxxx XX

ABSTRACT

We present a study of the 1173 sources brighter than $S_{1.4\,\mathrm{GHz}} = 120\,\mu$Jy detected over an area of $\simeq 1.4\,\mathrm{deg}^2$ in the Lockman Hole field. Exploiting the multi-band information available in this field for ∼79% of the sample, sources have been classified into radio loud (RL) active galactic nuclei (AGNs), star forming galaxies (SFGs) and radio quiet (RQ) AGNs, using a variety of diagnostics available in the literature. Exploiting the observed tight anti-correlations between IRAC band 1 or band 2 and the source redshift we could assign a redshift to 177 sources missing a spectroscopic measurement or a reliable photometric estimate. A Monte Carlo approach was used to take into account the spread around the mean relation. The derived differential number counts and luminosity functions at several redshifts of each population show a good consistency with models and with earlier estimates made using data from different surveys and applying different approaches. Our results confirm that below $\sim 300\,\mu$Jy SFGs+RQ AGNs overtake RL AGNs that dominate at brighter flux densities. We also confirm earlier indications of a similar evolution of RQ AGNs and SFGs. Finally, we discuss the angular correlation function of our sources and highlight its sensitivity to the criteria used for the classification.

Key words: galaxies: photometry – galaxies: active – galaxies: abundances – sub-millimetre: galaxies

1 INTRODUCTION

The advent of sub-mJy radio surveys has opened up a new view of the extragalactic radio sky (see De Zotti et al. 2010 and Padovani 2016 for reviews). At brighter flux densities the radio emission is almost exclusively of nuclear origin; such sources will be referred to as radio-loud active galactic nuclei (RL AGNs). Fainter sources comprise an increasing fraction of star-forming galaxies (SFGs) whose low-frequency radio emission is dominated by synchrotron radiation from relativistic electrons, accelerated by supernovae and their remnants, interacting with the galactic magnetic field. A substantial fraction of sources detected by deep radio surveys also contain active nuclei with weak radio emission, referred to as radio-quiet (RQ) AGNs. The origin of the radio emission of these objects is still debated since in most cases it is difficult to disentangle it from that of the host galaxies (see discussions in Bonato et al. 2017, Mancuso et al. 2017, Prandoni et al. 2018, Ceraj et al. 2018).

Studies of the composition of the faint radio source populations have been carried out exploiting deep radio surveys of fields for which a wealth of multifrequency data is available, such as the Extended Chandra Deep Field-South (ECDFS; Bonzini et al. 2013), the Cosmic Evolution Survey (COSMOS) field (Smolčić et al. 2017b) and the European Large-Area ISO Survey-North 1 (ELAIS-N1; Ocran et al. 2017, 2020a), among others. Despite the rapidly growing knowledge on this topic, considerable uncertainties remain and no general consensus has been reached. Analyses

⋆ matteo.bonato@inaf.it

© 2020 The Authors

of new samples are necessary to improve the statistics and to pinpoint the effect of different classification criteria.

The Lockman Hole (LH; Lockman et al. 1986, Lonsdale et al. 2003) field is one of the best-studied extra-galactic regions of the sky (see, e.g., Prandoni et al. 2018 for an overview of the available multi-band information). It is fully covered by the SERVS Data Fusion[1] (Vaccari 2015, Mauduit et al. 2012), including flux density measurements in the *Spitzer* IRAC band 1 (down to the detection limit of 2.21 μJy), band 2 (down to 2.7 μJy), band 3 (down to 40.8 μJy), band 4 (down to 44.4 μJy), in MIPS 24 μm band (down to 286.6 μJy) and in K_s band (up to Vega magnitude 21.5). The LH region was also the target of deep X-ray observations with the ROSAT, the XMM-*Newton* and the Chandra satellites (see Fig. 1 of Prandoni et al. 2018 and text for details).

Prandoni et al. (2018) presented new Westerbork Synthesis Radio Telescope (WSRT) 1.4 GHz mosaic observations, covering an area of 6.6 square degrees down to an rms noise of 11 μJy/beam, and the derived source counts. A comparison with existing radio source evolutionary models was also presented, based on a preliminary classification of the sources in the central 1.4 deg^2. In this paper, again focusing on the central $\sim$1.4 deg^2, we exploit the new radio data together with the available multi-band observations to get robust observational constraints on star formation and AGN activity of radio-detected sources, on their cosmic evolution and on their clustering properties, in preparation for the deeper and wider continuum extra-galactic surveys that will be carried out by the Square Kilometre Array (SKA).

In Sect. 2 we briefly introduce our sample, present a revised version of the source catalogue based on visual inspection of radio source/host galaxy identifications and describe the classification of the detected sources as either RL AGNs or SFGs or RQ AGNs. In Sect. 3 we present new estimates of the number counts of each sub-population, of luminosity functions in 13 redshift bins and of the 2-point angular correlation function. Our conclusions are summarized in Sect. 4. Throughout this paper, we adopt a flat ΛCDM cosmology with $\Omega_{\rm m} = 0.31$, $\Omega_\Lambda = 0.69$ and $h = H_0/100\,{\rm km\,s^{-1}\,Mpc^{-1}} = 0.67$ (Planck Collaboration 2015).

2 DATA AND CLASSIFICATION

2.1 Data

The sample we use is extracted from the full catalogue of radio sources published in Prandoni et al. (2018). The sub-region of interest, shown in Fig. 1, covers $\simeq$ 1.4 deg^2 at the center of the 1.4 GHz WSRT mosaic. This region is characterized by lowest, roughly uniform rms noise ($\sim$11 μJy/b) and is completely covered by the mentioned SERVS Data Fusion and by the UKIDSS-DXS deep K-band mosaic (Lawrence et al. 2007), which were extensively used for the source identification and classification processes. As described in Prandoni et al. (2018), only sources brighter than S$\geq$120 μJy (i.e. with S/N$\geq$10σ) were considered. This was

[1] http://www.mattiavaccari.net/df/

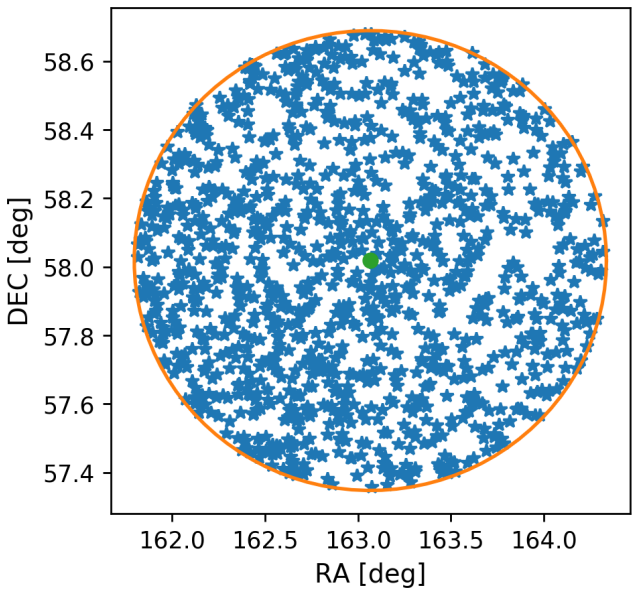


Figure 1. Spatial distribution (in equatorial coordinates, J2000) of the sources (the blue stars) analysed in this paper. The green central filled circle represents the center of the region.

motivated by the relatively poor resolution of the WSRT observations ($\sim$10 arcsec), in combination with the high number density of the confusion-limited SERVS data set, which prevented the search for counterparts to be pushed beyond 1.5$-$2 arcsec, to keep the fraction of misidentifications under control. This means that the identifications get progressively incomplete going to lower flux densities (where radio positional errors can be of the order of $\sim$1 arcsec). At 120 μJy the incompleteness was estimated to be $\sim$10$-$15 per cent (see Prandoni et al. 2018 for more details).

Table 1 reports the number of sources in the full catalogue and in the region of interest, as published in Prandoni et al. (2018). Using statistical criteria and (radio-only) visual inspection Prandoni et al. (2018) identified 183 multi-component source in the full catalogue and 45 in the inner region (all with S>120 μJy). These objects were attributed a flux density equal to the sum of flux densities of the individual components and the position of the centroid of component positions.

By taking advantage of the available optical/IR images, we further refined this number by inspecting radio/optical/IR overlays. After discarding obvious random pairs the number of confirmed multiple sources decreased to 76, 15 of which are located in the region of interest (see the updated numbers in Table 1). Correspondingly, the number of single-component sources with S>120 μJy in this region increased to 1158 so, in total, we have 1173 sources, 921 (908 single and 13 multiple) of which have an IRAC counterpart within 1.75 arcsec. This corresponds to an identification rate of $\sim$80% for the single sources and 87% for the multiple sources.

Nine hundred sources of our sample have flux density measurements in the *Spitzer* IRAC band 1, 919 in band 2, 620 in band 3 and 539 in band 4; 502 sources are detected in

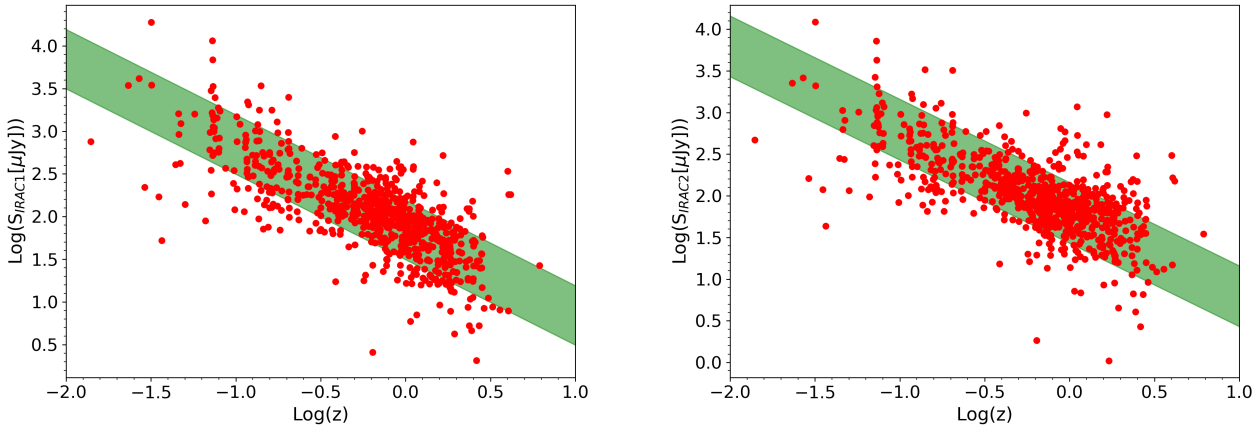


Figure 2. IRAC band 1 (left) and band 2 (right) flux densities vs. redshift for sources with spectroscopic or reliable photometric redshifts, in our sample. The green bands show the $2\,\sigma$ range around the mean relation $\log S_{\rm IRAC} = -\log z + c_{\rm IRAC}$, with $c_{\rm IRAC} = 1.79 \pm 0.36$ for band 2 and $= 1.84 \pm 0.35$ for band 1.

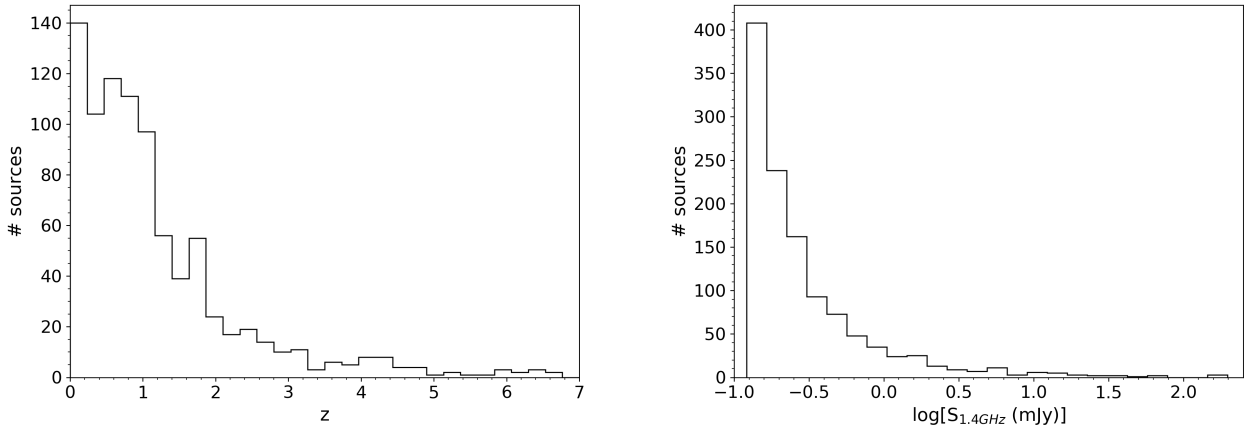


Figure 3. Redshift (left) and flux density (right) distributions for our sample. The redshifts of the IRAC identified sources without spectroscopic measurements or reliable photometric determinations were estimated using the mean relations with IRAC flux densities shown in Fig. 2 (see Sect. 2).

Table 1. Number of sources in the Prandoni et al. (2018) catalog and in the revised one (used in this paper).

Sample	N_{tot}	$N_{multiple}$
Full catalog (Prandoni et al. 2018)	5997	183
Inner S>120 μJy	1110	45
Revised full	6106	76
Inner S>120 μJy (IRAC identified)	1173 (921)	15 (13)

all the four IRAC bands. Moreover 914 sources have MIPS 24 μm fluxes and 829 have K_s magnitudes.

Using the recent "Herschel Extragalactic Legacy Project" (HELP[2]; Vaccari 2016) catalog (Shirley et al. 2019), we updated the redshift measurements[3] associated to our sources. We got reliable redshift determinations for 734 of our single sources (196 spectroscopic redshifts plus 538 photometric redshifts based on at least five optical bands). Moreover we have reliable redshifts for 10 multi-component sources. So, in total, 744 sources (∼63% of the sample) have reliable redshift determinations.

As shown by Fig. 2, IRAC band 1 and band 2 flux densi-

[2] https://herschel.sussex.ac.uk; https://hedam.lam.fr/HELP/

[3] The redshift estimations provided by Shirley et al. (2019), computed according to the Duncan et al. (2018b,a) techniques, constitute a refinement and an update of the measurements included in the SERVS Data Fusion and used by Prandoni et al. (2018).

ties are clearly anti-correlated with $\log(z)$[4] (Pearson's correlation coefficients of -0.75 and -0.69, respectively). The mean relations can be described as

$$\log S_{\rm IRAC} = c_{\rm IRAC} - \log z, \quad (1)$$

with $c_{\rm IRAC} = 1.84$ and a dispersion of 0.35 for band 1 and $c_{\rm IRAC} = 1.79$ with a dispersion of 0.36 for band 2.

For the source classification purposes described in the following sub-sections we have used a Monte Carlo approach, carrying out 10,000 simulations. In each simulation the 177 IRAC identified sources without a reliable redshift were attributed a value of z randomly drawn from a Gaussian distribution with mean given by eq. (1) for the source $\log S_{\rm IRAC}$ and the associated dispersion.

We have adopted the mean z and the dispersion from the IRAC band 2 for the 175 (out of 177) sources detected in this band. The other 2 sources were detected in band 1, and we used the corresponding values.

The Shirley et al. (2019) HELP catalogue also provided SFR determinations (see Małek et al. 2018 for the details of the adopted procedure) for 398 sources ($\simeq 34\%$ of the whole sample). SFR estimates for other $\simeq 395$ sources[5], $\sim 34\%$ of the sample, were obtained using the 24 μm flux density as a SFR indicator, using Fig. 6 of Battisti et al. (2015), valid up to $z \simeq 2.95$.

The use of the Battisti et al. (2015) 24 μm/SFR relation deserves a comment. Such relation was derived using a sample of SFGs and does not apply if a substantial fraction of the 24 μm flux is contributed by an AGN. This may be a serious limitation for our sample since at its 1.4 GHz flux density limit, $\sim 50\%$ of sources are expected to host an AGN (e.g., Bonzini et al. 2013). The AGN contribution leads to an overestimate of the inferred SFR; as a consequence the $L_{1.4\rm GHz}$/SFR ratio used to select RL AGNs (see sub-sect. 2.2) is underestimated and some RL AGNs are missed. However a closer look plays the problem somewhat down.

Elbaz et al. (2010) found that also AGNs associated to star forming galaxies have the same ratios of $L_{\rm IR}$ from 24 μm to $L_{\rm IR,tot}(> 30\mu{\rm m})$ as SFGs for $\log(L_{\rm IR\ from\ 24\mu m}/L_\odot) \lesssim 12.3$. On average, simulations yield IR luminosities above this limit for only 11% of sources for which we used the Battisti et al. (2015) relation. Of these, 32% are already classified as RL AGNs. Another 56%, i.e. 24, show signs of nuclear activity based on the diagnostics of sub-sect. 2.3; their SFRs might have been overestimated to the point that they are all misclassified RL AGNs. We have conservatively added the maximum number of misclassifications (24) to the error on the classification of RL and RQ AGNs. As we will see in the following sub-sections, this turns out to be a sub-dominant contribution.

As a counter-check we have assumed that 50% of the 24 μm flux of sources for which we used the Battisti et al. (2015) relation and were classified as RQ AGNs is of nuclear origin. Decreasing by a factor of 2 their SFRs, simulations give that, on average, 21 of them are reclassified as RL AGNs. This confirms that our previous estimate of the classification uncertainty is conservative.

The redshift and 1.4 GHz flux density distributions of our sample are shown in Fig. 3. The median values are $z \simeq 0.85$ and $S_{1.4\,\rm GHz} \simeq 0.208$ mJy.

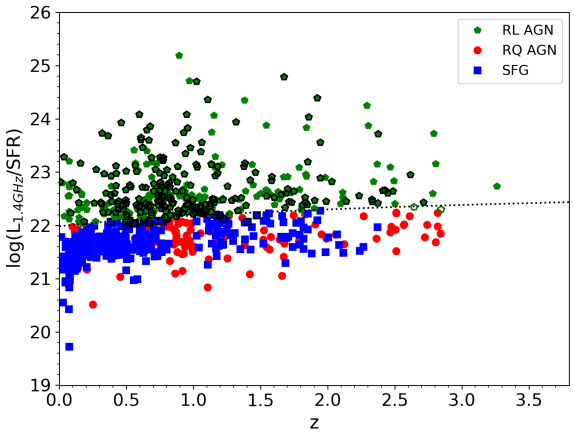


Figure 4. Radio-loudness diagnostics, $\log(L_{1.4\rm GHz}/{\rm SFR})$, versus z. The dotted black line represents the redshift-dependent (3σ) threshold given by Smolčić et al. (2017b): $\log(L_{1.4\rm GHz}/{\rm SFR}) = 21.984 \times (1+z)^{0.013}$, with $L_{1.4\rm GHz}$ in W Hz^{-1} and SFR in $M_\odot$ yr^{-1}. Pentagons, squares and circles are RL AGNs, SFGs and RQ AGNs, respectively. Filled pentagons refer to RL AGNs classified with $\log(L_{1.4\rm GHz}/{\rm SFR})$ above this threshold. Symbols with thick black borders represent sources for which no estimate of the SFR is available from the HELP catalogue and also miss the MIPS 24 μm flux density from which it could be derived. These objects were classified on the basis of their 5 σ upper limit at 24 μm (through the Battisti et al. 2015 relation, see sub-sect. 2.1). Whenever such upper limit was absent or did not allow a reliable classification we adopted the criterion by Magliocchetti et al. (2017, their eq. (1)) which classified them as RL AGNs; these objects are represented by open pentagons (note that most of the RL AGNs classified through the Magliocchetti et al. 2017 criterion don't have SFR estimates or upper limits and therefore are not present in this plot).

2.2 RL AGN classification

The multi-component sources were classified as RL AGNs. To select RL AGNs among the single-component sources we used two criteria. Whenever an estimate of the SFR was available (either from the HELP catalogue or derived from the 24 μm data) we classified as RL AGNs sources with radio luminosity to SFR ratios above the redshift-dependent threshold $\log(L_{1.4\rm GHz}/{\rm SFR}) = 21.984 \times (1+z)^{0.013}$, with $L_{1.4\rm GHz}$ in W Hz^{-1} and SFR in $M_\odot$ yr^{-1} (Smolčić et al. 2017b). This criterion is illustrated by Fig. 4.

For the other sources we adopted the Magliocchetti et al. (2017) criterion (their eq. 1), i.e. we classified as RL AGNs sources whose radio luminosity exceeds

$$\log L_{\rm cross}(z) = \begin{cases} 22.8 + z & \text{for } z \leq 1.8 \\ 24.6 & \text{for } z > 1.8 \end{cases} \quad (2)$$

[4] A relation between 3.6μm flux density and redshift was also found by Orenstein et al. (2019).
[5] The number is slightly different in different simulations, depending on the redshift assignations.

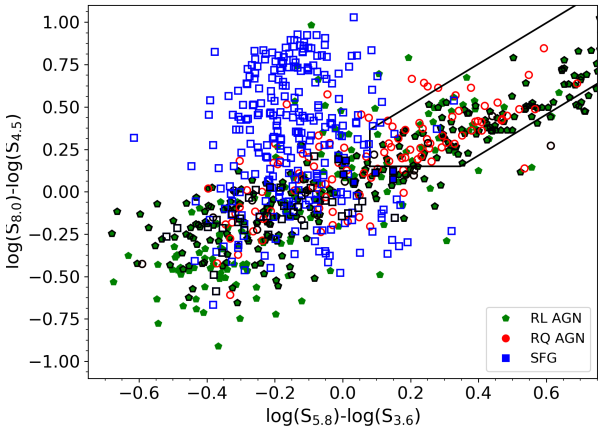


Figure 5. IRAC colour - colour diagram: $\log(S_{8.0\,\mu m}) - \log(S_{4.5\,\mu m})$ vs. $\log(S_{5.8\,\mu m}) - \log(S_{3.6\,\mu m})$ used to divide the non-RL AGNs between RQ AGNs and SFGs (see sub-sect. 2.3). The "RQ AGN region" (bounded by the solid black line) is defined by: $\log[S_{8.0\,\mu m}/S_{4.5\,\mu m}] \geq 0.15$; $\log[S_{5.8\,\mu m}/S_{3.6\,\mu m}] \geq 0.08$; $\log[S_{8.0\,\mu m}/S_{4.5\,\mu m}] \geq 1.21 \times \log[S_{5.8\,\mu m}/S_{3.6\,\mu m}] - 0.27$; $\log[S_{8.0\,\mu m}/S_{4.5\,\mu m}] \leq 1.21 \times \log[S_{5.8\,\mu m}/S_{3.6\,\mu m}] + 0.27$ (Donley et al. 2012). Circles, squares and pentagons represent RQ AGNs, SFGs and RL AGNs, respectively. The filled/open symbols refer to objects classified using this/another diagnostic or criterion (see text). Symbols with heavy black borders correspond to objects for which not all IRAC flux densities are available. The missing flux densities were replaced with their $5\,\sigma$ upper limits.

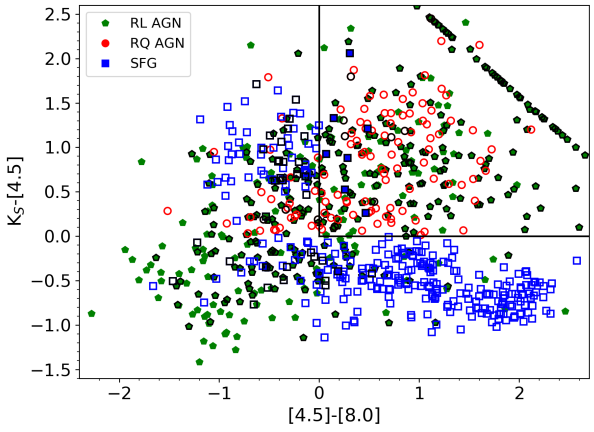


Figure 6. K_s–IRAC (KI) diagnostic plot. The K_s–[4.5] vs. [4.5]–[8.0] colours, with magnitudes converted to the AB system, are used to classify the non-RL AGN sources as either RQ AGNs or SFGs (see sub-sect. 2.3). The "RQ AGN region" (bounded by the solid black line) is defined by: $K_s - [4.5] > 0$; $[4.5] - [8.0] > 0$ (Messias et al. 2012). Circles, squares and pentagons represent RQ AGNs, SFGs and RL AGNs, respectively. Filled and open symbols represent sources classified with this or other diagnostics/criteria, respectively. Symbols with thick black borders refer to sources undetected in at least one of the three bands involved in this diagnostic, The missing magnitudes have been replaced by the corresponding $5\,\sigma$ detection limits.

Note that here radio luminosities are in $\mathrm{W\,Hz^{-1}}$ while in Magliocchetti et al. (2017) they are in $\mathrm{W\,Hz^{-1}\,sr^{-1}}$.

Using these criteria we identified 458 sources as RL AGNs, most of them ($\simeq$ 80%) through the first criterion. Adding the 15 multi-component sources we end up with a total of 473 RL AGNs.

2.3 SFG/RQ AGN classification

The 450 non-RL AGN (IRAC identified) sources were considered as either SFGs or RQ AGNs. To discriminate among the two populations, we adopted the redshift-dependent criterion discussed by Messias et al. (2012), that involves the K_s, 4.5, 8.0 and 24 μm AB magnitudes[6]. We classified sources as RQ AGNs when:

$$\begin{array}{ll} K_s - [4.5] > 0 & \text{for } z \leq 1; \\ [4.5] - [8.0] > 0 & \text{for } 1 < z \leq 2.5; \\ [8.0] - [24] > 1 & \text{for } z > 2.5. \end{array} \quad (3)$$

Sources missing either the K_s (for z$\leq$1) or the 24 μm (for $z > 2.5$) magnitudes were classified adopting either the IRAC colour-colour diagram ($\log S_{8.0\,\mu m} - \log S_{4.5\,\mu m}$ vs. $\log S_{5.8\,\mu m} - \log S_{3.6\,\mu m}$; Fig. 5) or the K_s–IRAC (KI) diagnostic plot (K_s–[4.5] vs. [4.5]–[8.0]; Fig. 6).

In the IRAC colour-colour diagram, the "RQ AGN region" is defined by (Donley et al. 2012):

$$\begin{array}{l} \log[S_{8.0\,\mu m}/S_{4.5\,\mu m}] \geq 0.15; \\ \log[S_{5.8\,\mu m}/S_{3.6\,\mu m}] \geq 0.08; \\ \log[S_{8.0\,\mu m}/S_{4.5\,\mu m}] \geq 1.21 \times \log[S_{5.8\,\mu m}/S_{3.6\,\mu m}] - 0.27; \\ \log[S_{8.0\,\mu m}/S_{4.5\,\mu m}] \leq 1.21 \times \log[S_{5.8\,\mu m}/S_{3.6\,\mu m}] + 0.27. \end{array} \quad (4)$$

In the KI diagnostic plot, the "RQ AGN region" is defined by (Messias et al. 2012):

$$\begin{array}{l} K_s - [4.5] > 0; \\ [4.5] - [8.0] > 0. \end{array} \quad (5)$$

None of these diagnostics could be applied to only 16 (IRAC identified) sources, which remained unclassified[7]. The IRAC and the KI diagnostics could be simultaneously applied only to very few sources ($\leq$ 3, the number varied in the different simulations[8]) and the classification always agreed.

A check of our classification was performed taking advantage of the XMM-*Newton* survey of the LH field (Brun-

[6] K_s Vega magnitudes were converted into AB magnitudes as $K_{s,\mathrm{AB}} = K_{s,\mathrm{Vega}} + 1.85$. Flux densities (in μJy) were converted into AB magnitudes through the relation: $\mathrm{ABmag} = -2.5 \times \log(S_\nu \times 10^{-29}) - 48.6$.

[7] The total number of unclassified sources, including the IRAC unidentified single-component sources (for which the application of our diagnostics was not possible as well), is 266 (i.e. 16+250). Actually, the total number of IRAC unidentified sources is 1173 − 921 = 252 (see sub-sect. 2.1. Two of them, however, are multi-component and were therefore classified as RL AGNs, as stated in sub-sect. 2.2.)

[8] The simulations, based on a Monte Carlo approach, are presented in sub-sect. 2.1.

Table 2. Sample of the catalogue content. The complete catalogue is available as supplementary material in the electronic version of the paper.

IAU name	RA J2000 [deg]	DEC J2000 [deg]	Classification	Class. rel. %	z	$S_{1.4GHz}$ [mJy]	σ [mJy]
LHWJ105237+573101	163.1549	57.5170	RL AGN	100	0.71	59.69	0.012
LHWJ105150+573244	162.9603	57.5456	RL AGN	100	0.19	16.18	0.012
LHWJ105427+573646	163.6127	57.6130	RL AGN	100	0.32	180.64	0.014
LHWJ104846+573750	162.1955	57.6308	RL AGN	100	0.92	0.49	0.011
LHWJ105337+574242	163.4060	57.7118	RL AGN	100	0.66	2.08	0.011
LHWJ105326+574544	163.3614	57.7623	RL AGN	100	0.87	7.02	0.010
LHWJ105243+574813	163.1810	57.8037	RL AGN	100	1.03	1.86	0.010
LHWJ105412+575651	163.5536	57.9476	RL AGN	100	0.64	2.86	0.010
LHWJ105027+581517	162.6132	58.2548	RL AGN	100	0.50	2.02	0.010
LHWJ105342+582108	163.4258	58.3525	RL AGN	100	-	0.93	0.010
LHWJ105351+582519	163.4656	58.4222	RL AGN	100	0.80	58.50	0.011
LHWJ105532+583156	163.8854	58.5323	RL AGN	100	-	1.75	0.011
LHWJ105116+583829	162.8190	58.6414	RL AGN	100	-	1.45	0.012
LHWJ105314+572411	163.3099	57.4032	SFG	100	1.69	0.12	0.011
LHWJ105217+572127	163.0735	57.3576	RQ AGN	100	0.05	0.21	0.011
LHWJ105237+572148	163.1559	57.3635	RQ AGN	100	0.48	0.16	0.011
LHWJ105308+572222	163.2835	57.3730	RL AGN	100	0.39	0.30	0.011
LHWJ104946+575140	162.4438	57.8612	RL AGN	100	0.04	0.16	0.010
LHWJ105120+572253	162.8347	57.3815	RL AGN	100	1.22	0.28	0.011
LHWJ105241+572320	163.1727	57.3890	RL AGN	100	1.06	1.86	0.011
LHWJ105158+572329	162.9955	57.3916	RL AGN	100	-	0.24	0.011
LHWJ105305+572330	163.2721	57.3919	RQ AGN	100	0.99	0.15	0.011
LHWJ105254+572341	163.2261	57.3950	RL AGN	100	0.76	0.20	0.011
LHWJ105356+572355	163.4837	57.3986	RQ AGN	100	1.35	0.13	0.011
LHWJ105348+572358	163.4520	57.3996	SFG	100	1.67	0.12	0.011
LHWJ105031+572401	162.6314	57.4003	RL AGN	100	-	0.13	0.012
LHWJ105406+572413	163.5254	57.4039	RQ AGN	100	0.77	0.16	0.012
LHWJ105053+572427	162.7223	57.4076	SFG	100	0.40	0.31	0.012
LHWJ105239+572432	163.1651	57.4089	RQ AGN	100	1.11	0.16	0.011
LHWJ105023+572439	162.5971	57.4108	SFG	100	1.19	0.29	0.011
LHWJ105242+572444	163.1765	57.4124	SFG	100	0.08	0.27	0.011
LHWJ105314+572449	163.3085	57.4138	RL AGN	100	0.69	0.17	0.011
LHWJ105212+572453	163.0522	57.4148	SFG	100	0.50	0.23	0.011
LHWJ105301+572521	163.2570	57.4227	RL AGN	100	0.57	0.29	0.011
LHWJ105008+572514	162.5349	57.4207	RQ AGN	100	2.51	0.16	0.011
LHWJ105356+572516	163.4840	57.4211	SFG	100	0.50	0.12	0.011
LHWJ105343+572531	163.4314	57.4253	RL AGN	100	0.75	0.31	0.011
LHWJ105049+572527	162.7054	57.4243	SFG	100	0.37	0.14	0.011
LHWJ105035+572532	162.6460	57.4258	RL AGN	94	-	0.20	0.011
LHWJ105421+572544	163.5883	57.4290	RQ AGN	100	0.20	1.06	0.012
LHWJ105232+572543	163.1370	57.4286	RQ AGN	100	0.56	0.14	0.011
LHWJ105403+572553	163.5159	57.4314	RQ AGN	100	2.82	0.18	0.012
LHWJ105359+572559	163.4995	57.4333	RQ AGN	100	2.82	0.24	0.012
LHWJ105035+572607	162.6490	57.4355	SFG	100	0.36	0.17	0.011
LHWJ105149+572635	162.9582	57.4432	RL AGN	100	1.14	0.27	0.010
LHWJ105032+572646	162.6362	57.4463	RL AGN	100	-	0.62	0.011
LHWJ105113+572654	162.8060	57.4484	RQ AGN	100	0.63	0.29	0.010
LHWJ105351+572700	163.4662	57.4501	RQ AGN	100	0.92	0.21	0.011
LHWJ105204+572657	163.0170	57.4494	x	0	1.48	0.15	0.011
LHWJ105104+572719	162.7707	57.4553	RL AGN	75	-	0.20	0.010
...	...	...	...	...	...	...	...

Notes.

1. In the case of extended sources, $S_{1.4GHz}$ is the flux density measured by summing all the pixels above a $3\,\sigma$ threshold (see Prandoni et al. 2018 for details).

2. σ is the local rms noise value.

3. For IRAC identified sources lacking a reliable redshift determination we give the reliability of the classification (Class. rel.) defined as the percentage of simulations described in sub-sect. 2.1 yielding such classification.

4. The X-ray analysis (see sub-sect. 2.3) shows that the number of SFGs should be corrected by a factor of ∼0.88. However, this correction has only a statistical meaning and cannot be done source by source. In the table we have corrected the classification (from SFG to RQ AGN) of only the three sources in the XMM-*Newton* survey with $L_X > 10^{42}\,\mathrm{erg\,s^{-1}}$.

ner et al. 2008) which covers a small fraction ($\sim 10\%$) of our field. In the overlapping area there are 121 of our sources, 46 classified as RL AGNs, 24 as SFGs, 24 as RQ AGNs and 27 unclassified. Using a $4''$ search radius (the XMM-*Newton* positional errors are generally $< 1''$ but in some cases reach $2.3''$), we found 32 matches: 11 classified as RL AGNs, 9 as RQ AGNs, 8 as SFGs and 4 unclassified. Three "SFGs" turned out to have 2–10 keV luminosities $L_X > 10^{42}\,\mathrm{erg\,s^{-1}}$. The X-ray luminosity associated to star-formation rarely exceeds $L_X = 10^{41.5}\,\mathrm{erg\,s^{-1}}$ (Ranalli et al. 2003; Lehmer et al. 2010); hence such sources are most likely misclassified RQ AGNs. The other 5 have L_X in the range $7{\times}10^{38} - 4{\times}10^{41}$erg/s, hence compatible with the SFG classification, although the presence of a low-luminosity AGN cannot be excluded.

Based on this result, we have corrected the number of SFGs by a factor $(24-3)/24 \simeq 0.88$, thus decreasing it from 310 to 271. Since the radio-loudness diagnostics indicate that these X-ray sources are not RL, we reclassify them as RQ AGNs. If we conservatively consider as uncertain the classification of the 5 sources with X-ray luminosity compatible with the SFG classification, the contribution to the error budget of the classification uncertainty is $5/(24-3) \simeq 24\%$. After this correction the result of the classification is 271 ± 74 SFGs and 163 ± 74 RQ AGNs.

Note that the contributions to the global error of uncertainties associated to the 24 μm–SFR conversion is subdominant.

The source catalogue, including our classification, is available as supplementary material in the electronic version of the paper. The catalogue gives the IAU name, the equatorial coordinates (J2000), the source classification, its redshift (if available), the 1.4 GHz flux density and the rms. An example of the content of the catalogue is given in Table 2.

3 RESULTS

3.1 Number counts

Our estimates of the Euclidean normalized differential number counts of RL AGNs, RQ AGNs and SFGs, and the total are reported in Tab. 3 and displayed in Fig. 7. The unclassified and/or unidentified sources have been distributed among the three populations in proportion to their numbers in each flux density bin.

The number counts of SFGs and of RQ AGNs were corrected for misclassifications based on the X-ray data, as described above. The uncertainties on the number counts are the sum in quadrature of Poisson errors and of the variance in the simulations. In the case of SFGs and RQ AGNs, we have also taken into account the conservative classification uncertainty (sub-sect. 2.3).

Obviously the adoption of the same correction factor for all flux density bins is a rough fix, but it is the best we can do since the very poor statistics prevents any possibility of a more refined, and realistic, treatment. This is taken into account applying a conservative error estimate, including the classification uncertainty.

In the left panel of Fig. 7 our estimates are compared with the models by Bonato et al. (2017), Mancuso et al. (2017) and Wilman et al. (2008). The models by Wilman et al. (2008) and by Bonato et al. (2017) provide a good fit of our observational determination of the counts of RL AGNs. The model by Bonato et al. (2017), which does not distinguish between SFGs and RQ AGNs, reproduces quite well also their summed counts. Wilman et al. (2008) slightly under-predict the counts of both RQ AGNs and SFGs, and of the total population as well, as noted also by Prandoni et al. (2018). The model by Mancuso et al. (2017) nicely agrees with our counts.

As illustrated by the right-hand panel of Fig. 7, our estimates of the counts of each population agree, within the errors, with those by Padovani et al. (2015) and Smolčić et al. (2017b) who used different samples and different approaches. These studies converge in indicating that RL AGNs dominate the 1.4 GHz counts above 200–300 μJy, while SFGs+RQ AGNs take over at fainter flux densities. The counts of RQ AGNs are approximately parallel to those of SFGs, indicating similar evolution, as previously pointed out by Padovani et al. (2015). Our estimates give surface densities of RQ AGNs only slightly below those of SFGs, at variance with Padovani et al. (2015) who found abundances of RQ AGNs lower than those of SFGs by factors of 2 to 3.

3.2 Luminosity functions

The calculation of 1.4 GHz luminosities from the measured flux densities

$$L_\nu = \frac{4\pi d_L^2 S_\nu}{K(L_\nu, z)}, \tag{6}$$

d_L being the luminosity distance, requires the evaluation of the K-correction

$$K(L_\nu, z) = \frac{(1+z)L[\nu(1+z)]}{L(\nu)}. \tag{7}$$

We have adopted simple power-law spectra, $S_\nu \propto \nu^{-\alpha}$ so that $K \propto (1+z)^{1-\alpha}$, with $\alpha = 0.8$ for SFGs (Condon 1992; Ibar et al. 2010) and RQ AGNs and $\alpha = 0.75$ for RL AGNs (e.g., Smolčić et al. 2017a). The latter choice is obviously not appropriate for flat-spectrum radio sources, which are however expected to be a small minority.

The luminosity function (LF) in the k-th redshift bin was derived using the $1/V_{\max}$ method (Schmidt 1968):

$$\frac{dN(L_j, z_k)}{d\log L} = \frac{1}{\Delta \log L} \sum_{i=1}^{N_j} \frac{w_i}{V_{\max,i}(z_k)} \tag{8}$$

where z_k is the bin center and the sum is over all the N_j sources with luminosity in the range $[\log L_j - \Delta\log L/2, \log L_j + \Delta \log L/2]$ within the redshift bin. We chose $\Delta z = 0.2$ for $z < 2$ and $\Delta z = 0.4$ for $z > 2$. These redshift bins are large enough to have a sufficient statistics and narrow enough to allow us to neglect evolutionary corrections within the bin. The values of $\Delta \log L$ are different in different redshift bins (see Table 4); they are larger in the poorly populated luminosity ranges.

The weights w_i take into account the incompleteness in the identifications. It was evaluated from the ratio between the $\log(S_{1.4\,GHz})$ distributions of all the sources and of the identified sources, in each bin. The $V_{\max,i}$ is the comoving volume, within the solid angle of the survey, enclosed between the lower limit, $z_{\min}$, of the bin and the minimum

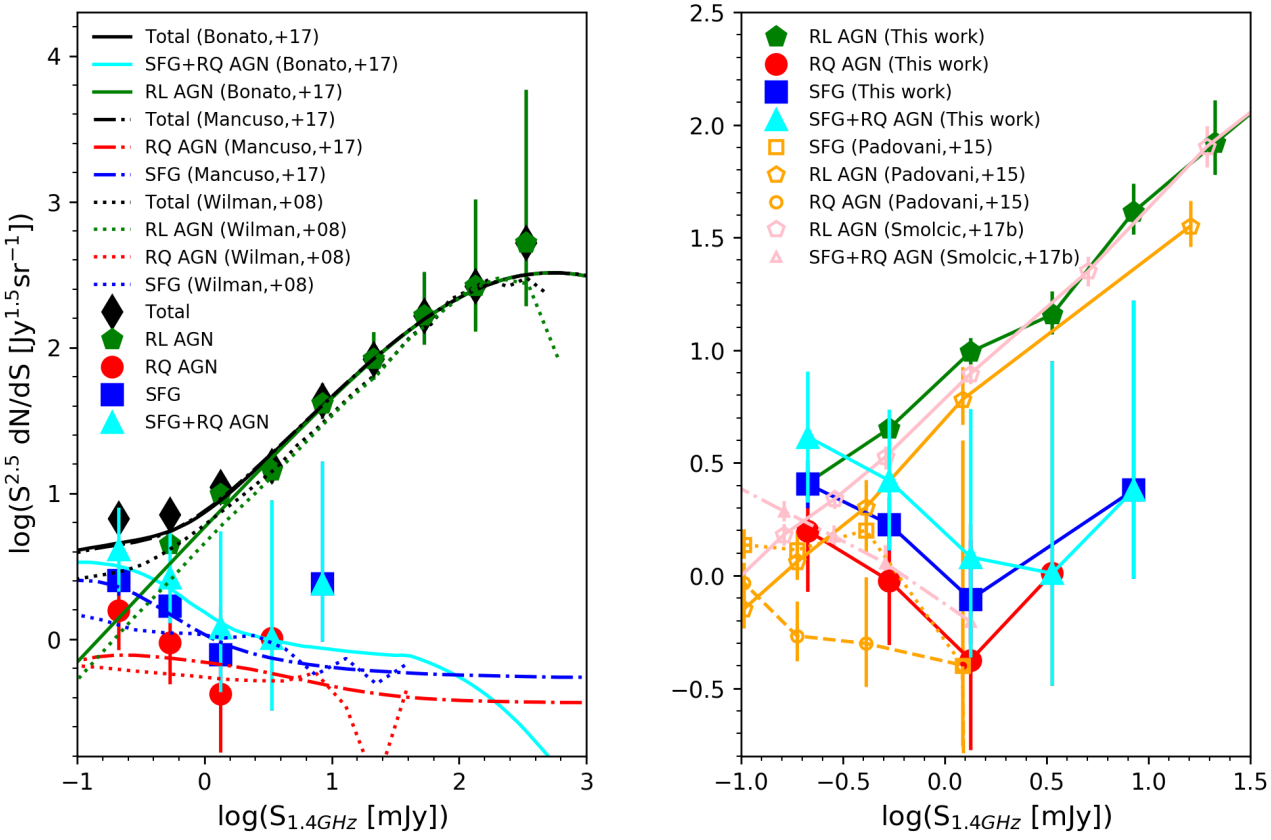


Figure 7. Comparison of our estimate of the number counts at 1.4 GHz of RL AGNs, RQ AGNs, SFGs, RQ AGNs+SFGs and total, with models and with other estimates (left and right panel, respectively). Models are from Bonato et al. (2017, RL AGNs, SFGs+RQ AGNs and total), Mancuso et al. (2017, SFGs, RQ AGNs and total) and Wilman et al. (2008, RL AGNs, SFGs, RQ AGNs and total). The Tiered Radio Extragalactic Continuum Simulation (T-RECS) counts Bonaldi et al. (2019), not shown, are very close to the Bonato et al. (2017) ones. The observational estimates are from Padovani et al. (2015), Smolčić et al. (2017b) and from the present work. The lines connecting the points (on the right panel) are only meant to guide the eye.

Table 3. Estimates of the 1.4 GHz Euclidean normalized differential counts, $S^{2.5}dN/dS[\mathrm{Jy}^{1.5}\mathrm{sr}^{-1}]$, for the RL AGN, SFG and RQ AGN populations, and total. On the right of the counts we give the number, N, of sources in each bin. It includes the contributions of unidentified and unclassified sources as well as the correction for the misclassification indicated by X-ray data (for SFGs and RQ AGNs). The errors are dominated by classification uncertainties. See sub-sect. 3.1.

$\log S$ [mJy]	$\log(\mathrm{Counts_{TOT}})$ $[\mathrm{Jy}^{1.5}\mathrm{sr}^{-1}]$	$\mathrm{N_{TOT}}$	$\log(\mathrm{Counts_{RL\,AGN}})$ $[\mathrm{Jy}^{1.5}\mathrm{sr}^{-1}]$	$\mathrm{N_{RL\,AGN}}$	$\log(\mathrm{Counts_{SFG}})$ $[\mathrm{Jy}^{1.5}\mathrm{sr}^{-1}]$	$\mathrm{N_{SFG}}$	$\log(\mathrm{Counts_{RQ\,AGN}})$ $[\mathrm{Jy}^{1.5}\mathrm{sr}^{-1}]$	$\mathrm{N_{RQ\,AGN}}$
-0.67	$0.83^{+0.02}_{-0.02}$	805	$0.41^{+0.03}_{-0.03}$	309	$0.41^{+0.11}_{-0.11}$	306	$0.20^{+0.27}_{-0.27}$	190
-0.27	$0.85^{+0.03}_{-0.03}$	216	$0.65^{+0.05}_{-0.04}$	136	$0.23^{+0.12}_{-0.12}$	51	$-0.02^{+0.29}_{-0.28}$	29
0.13	$1.04^{+0.05}_{-0.05}$	84	$0.99^{+0.06}_{-0.05}$	75	$-0.10^{+0.26}_{-0.20}$	6	$-0.37^{+0.60}_{-0.40}$	3
0.53	$1.19^{+0.10}_{-0.08}$	29	$1.16^{+0.10}_{-0.09}$	27	–	–	$0.01^{+0.94}_{-0.50}$	2
0.93	$1.64^{+0.12}_{-0.09}$	21	$1.61^{+0.12}_{-0.10}$	20	$0.38^{+0.84}_{-0.39}$	1	–	–
1.33	$1.92^{+0.19}_{-0.14}$	10	$1.92^{+0.19}_{-0.14}$	10	–	–	–	–
1.73	$2.22^{+0.30}_{-0.19}$	5	$2.22^{+0.30}_{-0.20}$	5	–	–	–	–
2.13	$2.42^{+0.59}_{-0.31}$	2	$2.42^{+0.59}_{-0.31}$	2	–	–	–	–
2.53	$2.72^{+1.05}_{-0.43}$	1	$2.72^{+1.05}_{-0.43}$	1	–	–	–	–

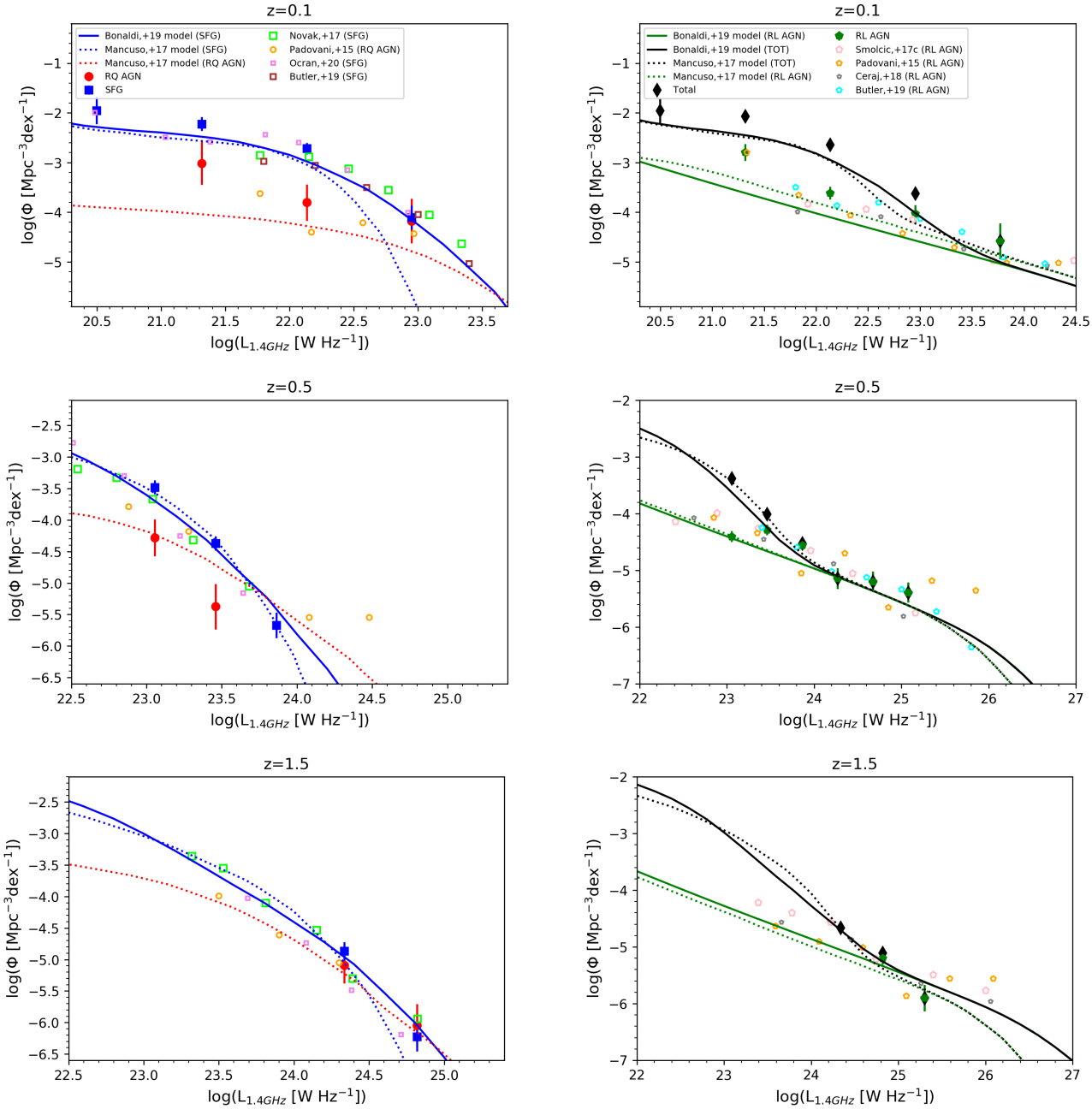


Figure 8. Comparison of our estimates of the LFs of non-radio excess sources (SFGs and RQ AGNs) and RL AGNs (left and right panels, respectively) with those of SFGs by Novak et al. (2017), Butler et al. (2019, including high-excitation sources whose radio emission likely originates from star formation) and Ocran et al. (2020b), of RQ AGNs by Padovani et al. (2015) and of RL AGNs by Padovani et al. (2015), Smolčić et al. (2017c), Ceraj et al. (2018) and Butler et al. (2019). The estimates by Ocran et al. (2020b) have been converted from 610 MHz to 1.4 GHz using the spectral index ($\alpha = 0.8$) used by these authors. Also shown, for comparison, are the models by Mancuso et al. (2017) for SFGs, RQ and RL AGNs and by Bonaldi et al. (2019) for SFGs and RL AGNs.

between the upper limit, $z_{\rm max}$, and the maximum redshift at which the source is above both the IRAC 2 (44 μJy) and the radio (120 μJy) flux limits.

The LFs of SFGs and of RQ AGNs were further corrected for misclassifications based on the X-ray data, as described above. In the present data situation the best we could do was to apply the correction factors of sub-sect. 2.3 to the normalizations at all redshifts, including the corresponding uncertainty in the error budget. Although the true correction factors are most likely redshift-dependent, they are within our conservative error bars.

The Poisson error on $dN(L_j, z_k)/d\log L$ was estimated as:

$$\sigma_{j,k} = \left\{ \sum_{i=1}^{N_j} \frac{w_i^2}{[V_{{\rm max},i}(z_k)]^2} \right\}^{1/2} . \quad (9)$$

For the SFG and the RQ AGN populations the uncertainty is the sum in quadrature of Poisson errors, of classification uncertainties and of the fluctuations of the number of sources in each redshift and luminosity bin obtained from simulations. For the RL AGNs and the total population, the uncertainty takes into account the variance in the simulations and the Poisson errors.

Our estimates of the 1.4 GHz LFs for each source population are listed in Table 4. Some examples are shown and compared with other estimates and with models in Fig. 8. RL AGNs have LFs much flatter than SFGs, so that the two populations dominate at high and low radio luminosities, respectively. The transition luminosity increases with z from $L_{1.4\,\mathrm{GHz}} \simeq 10^{23.2}$ to $\simeq 10^{24}\,\mathrm{W\,Hz^{-1}}$.

At all redshifts the RQ AGNs have space densities comparable to SFGs for $L_{1.4\,\mathrm{GHz}} > 10^{24}\,\mathrm{W\,Hz^{-1}}$. The redshift independence of the density ratios of the two populations implies similar evolution, as previously noted by Padovani et al. (2015). At lower radio luminosities, however, SFGs outnumber RQ AGNs by a substantial factor. Part of the difference may be due to the difficulty of pinpointing faint AGNs.

The consistency with earlier estimates and with model predictions is generally good.

3.3 Clustering

Measurements of the clustering properties of extragalactic source populations are an efficient way to gain information on the relationship between their distribution and that of dark matter matter halos, hence on their formation history and on their environment (Peebles 1980). The radio band has important advantages over the optical band where most clustering studies have been carried out. It is better suited to investigate the large scale structure at high redshift thanks to the strong cosmological evolution of radio loud AGNs and to the immunity to dust obscuration. Also, the survey speed is generally higher in the radio making much easier to uniformly cover large areas of the sky. This has motivated many clustering studies at various radio frequencies and to different depths (e.g. Lindsay et al. 2014; Magliocchetti et al. 2017; Hale et al. 2018, 2019; Rana & Bagla 2019; Chakraborty et al. 2020).

We have computed the 2-point angular correlation function, $w(\theta)$, using the public Python package AstroML (Vanderplas et al. 2012; Ivezić et al. 2014) and specifically the "bootstrap_two_point_angular" function[9]. The $w(\theta)$ is computed exploiting the Landy-Szalay estimator (Landy & Szalay 1993):

$$w(\theta) = \frac{DD(\theta) - 2DR(\theta) + RR(\theta)}{RR(\theta)}, \qquad (10)$$

where $DD(\theta)$ is the real number of source pairs separated by an angle θ, $RR(\theta)$ is the number of pairs expected in the case of a random distribution and $DR(\theta)$ is the number of data-random pairs. We limited ourselves to angular scales > 100 arcsec since smaller scales may be affected by an over/under-correction for multiple source components. The results are presented in Fig. 9 where they are also compared with previous estimates.

The most straightforward comparison is that with the estimate by Magliocchetti et al. (2017) who used a sample of similar size (they have 968 sources) and depth to ours, selected at the same frequency. To put ourselves on an exactly equal footing we have adopted their 1.4 GHz flux density threshold (0.15 mJy).

On the scales probed by our sample, the $w(\theta)$ is well described by a power law, $w(\theta) = A(\theta/\mathrm{deg})^{1-\gamma}$ with $A \simeq (0.012 \pm 0.005)$ and $\gamma = 1.957 \pm 0.151$. Our estimate is higher than that by Magliocchetti et al. (2017), although consistent with it within the errors. Part of the difference may be due to sample variance.

Our global redshift distribution of sources with $S_{1.4\,\mathrm{GHz}} \geq 150\,\mu$Jy is similar to that by Magliocchetti et al. (2017, Fig. 10) who have a higher fraction of spectroscopic plus reliable photometric redshifts ($\simeq 92\%$). This lends support to the validity of our statistical procedure for redshift assignments.

The determination of the correlation function of each source population is hampered by the poor statistics which prevents a simultaneous estimate of both A and γ. Fixing γ to the best fit value for the full sample ($\gamma = 1.957$), we get the results shown in the right-hand panel of Fig. 9. This figure shows that the difference with Magliocchetti et al. (2017) mostly arises from RL AGNs, for which our estimate is significantly higher.

The origin of this difference can be traced back to the criteria used to separate "AGNs" from "SFGs". The separation made by Magliocchetti et al. (2017) relied purely on radio luminosity, independently of the SFR. The result is that, except for a small secondary peak at $z \simeq 1.9$, their "SFGs" are at $z \leq 0.8$ while in our case a substantial fraction of them is located at $0.6 \leq z \leq 1.5$ with a tail extending up to $z \simeq 3$, mostly populated by RQ AGNs.

According to our estimate, RL AGNs and SFGs have correlation functions with amplitudes $A = 0.013 \pm 0.001$ and 0.008 ± 0.001, respectively. In contrast, Magliocchetti et al. (2017) found a somewhat stronger clustering for "SFGs" than for "AGNs".

The other determinations of the clustering amplitude shown in Fig. 9 are consistent within the errors, with our results, although somewhat lower. The comparison however has to be taken with caution since they refer to surveys at different frequencies and/or of different depths. In fact, the mixture of source populations (e.g. the relative fractions of steep- and flat-spectrum sources) vary with frequency and the redshift distributions vary with the survey depth. Indeed, variation of the clustering amplitude with flux density limit has been reported by Rana & Bagla (2019).

Lindsay et al. (2014) studied the clustering properties of sources in the Faint Images of the Radio Sky at Twenty-cm (FIRST) survey at 1.4 GHz, with a flux limit of 1 mJy, several times higher than that of our sample. Hale et al. (2018) investigated a sample selected at 3 GHz flux limited at $\simeq 13\,\mu$Jy. Hale et al. (2019) analyzed a sample of sources brighter than ~ 2 mJy at 144 MHz. Rana & Bagla (2019) used a shallow large-area sample selected at 150 MHz and used various flux density thresholds (50, 60, 100 and 200 mJy). Chakraborty et al. (2020) used 400 MHz obser-

[9] https://www.astroml.org/modules/generated/astroML.correlation.bootstrap_two_point_angular.html

Table 4. Estimates of the 1.4 GHz luminosity function, $\Phi = dN/(d\log L\, dV)$[Mpc^{-3}], for RL AGNs, SFGs and RQ AGNs, and total. On the right of the luminosity functions we give the number, N, of sources in each bin. It includes the contributions of unidentified and unclassified sources as well as the correction for the misclassification indicated by X-ray data (for SFGs and RQ AGNs). The errors are dominated by classification uncertainties.

$\log L$ [W Hz^{-1}]	$\log(\Phi_{\rm TOT})$ [Mpc^{-3} dex^{-1}]	$N_{\rm TOT}$	$\log(\Phi_{\rm RL\,AGN})$ [Mpc^{-3} dex^{-1}]	$N_{\rm RL\,AGN}$	$\log(\Phi_{\rm SFG})$ [Mpc^{-3} dex^{-1}]	$N_{\rm SFG}$	$\log(\Phi_{\rm RQ\,AGN})$ [Mpc^{-3} dex^{-1}]	$N_{\rm RQ\,AGN}$
				z = 0– 0.2				
20.50	-1.95 ± 0.25	4	–	–	-1.95 ± 0.27	4	–	–
21.32	-2.06 ± 0.08	40	-2.79 ± 0.17	7	-2.22 ± 0.14	30	-3.01 ± 0.43	3
22.13	-2.64 ± 0.05	96	-3.61 ± 0.13	11	-2.72 ± 0.12	78	-3.80 ± 0.36	7
22.95	-3.62 ± 0.12	14	-4.03 ± 0.17	5	-4.10 ± 0.24	5	-4.18 ± 0.45	4
23.77	-4.58 ± 0.36	2	-4.58 ± 0.36	2	–	–	–	–
				z = 0.2 – 0.4				
22.61	-2.94 ± 0.11	96	-4.77 ± 0.17	6	-3.00 ± 0.16	78	-3.90 ± 0.38	12
23.51	-4.26 ± 0.10	22	-4.52 ± 0.14	12	-4.79 ± 0.19	7	-5.08 ± 0.39	3
24.41	-5.25 ± 0.28	2	-5.25 ± 0.28	2	–	–	–	–
25.31	-5.62 ± 0.39	1	-5.62 ± 0.39	1	–	–	–	–
				z = 0.4 – 0.6				
23.06	-3.37 ± 0.04	67	-4.40 ± 0.10	10	-3.48 ± 0.11	47	-4.28 ± 0.29	10
23.46	-4.01 ± 0.05	31	-4.29 ± 0.09	13	-4.37 ± 0.11	17	-5.37 ± 0.36	1
23.86	-4.52 ± 0.07	12	-4.56 ± 0.07	11	-5.67 ± 0.20	1	–	–
24.27	-5.14 ± 0.18	2	-5.14 ± 0.18	2	–	–	–	–
24.67	-5.20 ± 0.18	1	-5.20 ± 0.18	1	–	–	–	–
25.08	-5.39 ± 0.18	2	-5.39 ± 0.18	2	–	–	–	–
				z = 0.6 – 0.8				
23.49	-3.69 ± 0.04	77	-4.38 ± 0.08	18	-3.97 ± 0.12	39	-4.28 ± 0.28	20
23.98	-4.37 ± 0.06	28	-4.41 ± 0.06	25	–	–	-5.45 ± 0.31	3
24.47	-4.75 ± 0.07	13	-4.75 ± 0.08	13	–	–	–	–
24.96	-5.01 ± 0.10	7	-5.01 ± 0.10	7	–	–	–	–
25.94	-5.59 ± 0.15	2	-5.59 ± 0.15	2	–	–	–	–
				z = 0.8 – 1.0				
24.00	-4.15 ± 0.08	81	-4.58 ± 0.09	34	-6.21 ± 0.38	1	-4.36 ± 0.29	46
24.83	-5.17 ± 0.13	11	-5.22 ± 0.14	10	–	–	-6.12 ± 0.45	1
25.67	-5.65 ± 0.21	4	-5.65 ± 0.21	4	–	–	–	–
26.50	-6.24 ± 0.36	1	-6.24 ± 0.36	1	–	–	–	–
				z = 1.0 – 1.2				
24.20	-4.49 ± 0.07	54	-4.83 ± 0.10	24	-4.94 ± 0.16	19	-5.22 ± 0.31	11
25.02	-5.32 ± 0.13	9	-5.32 ± 0.13	9	–	–	–	–
25.85	-5.60 ± 0.24	3	-5.60 ± 0.24	3	–	–	–	–
				z = 1.2 – 1.4				
24.24	-4.41 ± 0.11	31	-5.33 ± 0.15	8	-4.53 ± 0.17	17	-5.33 ± 0.31	6
24.86	-5.69 ± 0.21	2	-5.69 ± 0.21	2	–	–	–	–
26.11	-6.24 ± 0.27	1	-6.24 ± 0.27	1	–	–	–	–
				z = 1.4 – 1.6				
24.34	-4.66 ± 0.09	21	–	–	-4.87 ± 0.15	10	-5.09 ± 0.28	11
24.82	-5.11 ± 0.10	8	-5.20 ± 0.11	6	-6.22 ± 0.23	1	-6.05 ± 0.34	1
25.30	-5.90 ± 0.23	2	-5.90 ± 0.23	2	–	–	–	–
				z = 1.6 – 1.8				
24.68	-4.87 ± 0.10	29	-5.42 ± 0.20	6	-5.19 ± 0.17	14	-5.48 ± 0.32	9
25.55	-6.21 ± 0.39	1	-6.21 ± 0.39	1	–	–	–	–
26.42	-6.14 ± 0.27	2	-6.14 ± 0.27	2	–	–	–	–
				z = 1.8 – 2.0				
24.51	-4.76 ± 0.06	16	-5.18 ± 0.10	4	-5.19 ± 0.13	7	-5.38 ± 0.29	5
24.85	-5.50 ± 0.09	4	–	–	-5.50 ± 0.13	4	–	–
				z = 2.0 – 2.4				
24.78	-5.49 ± 0.12	12	-6.28 ± 0.33	2	-5.94 ± 0.19	4	-5.82 ± 0.30	6
26.61	-6.62 ± 0.26	1	-6.62 ± 0.27	1	–	–	–	–
				z = 2.4 – 2.8				
24.94	-5.51 ± 0.10	9	-6.09 ± 0.24	2	–	–	-5.64 ± 0.28	7
26.23	-6.41 ± 0.19	1	-6.41 ± 0.19	1	–	–	–	–
				z = 2.8 – 3.2				
25.02	-6.04 ± 0.21	3	–	–	–	–	-6.04 ± 0.30	3
25.45	-6.02 ± 0.20	1	-6.02 ± 0.20	1	–	–	–	–

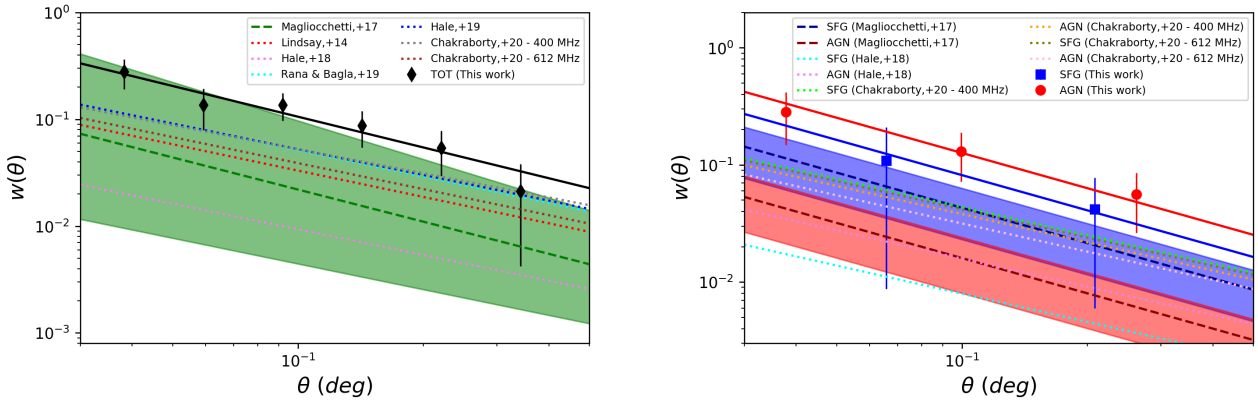


Figure 9. Two-point angular correlation function, $w(\theta)$, derived from our catalog (the datapoints), compared to the results of Magliocchetti et al. (2017) (the coloured bands). The left and the right panels show, respectively, the $w(\theta)$ for the full $S_{1.4\,\mathrm{GHz}}$ sample and for "SFGs" and RL AGNs ("AGN") separately. The poor statistics does not allow us to derive separate correlation functions for SFGs and RQ AGNs. Also Magliocchetti et al. (2017) have considered the two populations together. We show only bins where we have sufficient statistics and at angular scales >100 arcsec (i.e. larger than the maximum angular separation used to identify multi-component sources). We have also added, for comparison, the best fit $w(\theta)$ reported by other studies: Lindsay et al. (2014), Hale et al. (2018), Hale et al. (2019), Rana & Bagla (2019) and Chakraborty et al. (2020). The results for "SFG" and "AGN" by Hale et al. (2018) are the fits given in their Table 1.

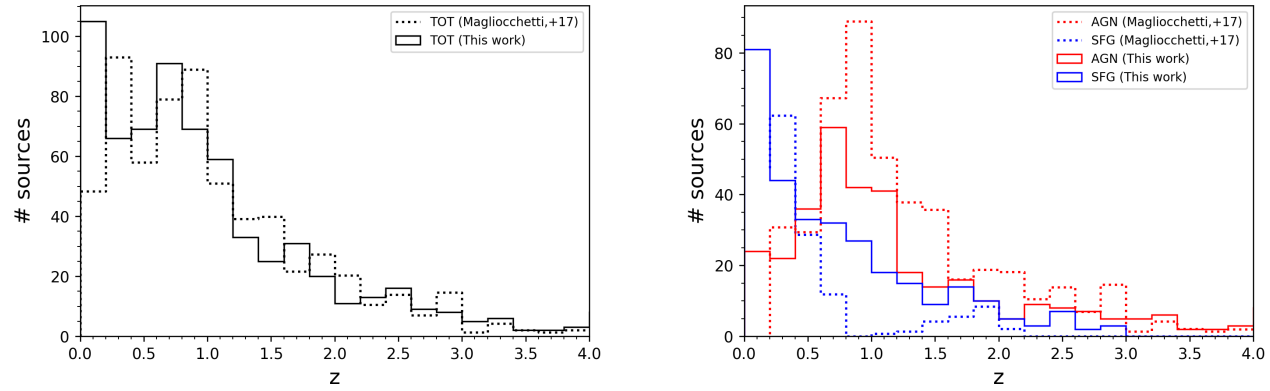


Figure 10. Comparison between the redshift distributions of our sources brighter than 150 μJy and the Magliocchetti et al. (2017) one, normalized to the area of our survey (i.e. $\sim$1.4 deg^2). The left panel shows the global redshift distributions while the right one shows those of "AGNs" and of "SFGs" (see caption of Fig. 9) separately.

vations flux limited at 100 μJy and 612 MHz data down to 50 μJy.

4 CONCLUSIONS

We have exploited the rich multi-band information available on the LH field to classify radio sources with $S_{1.4\,\mathrm{GHz}} > 120\,\mu$Jy detected by the deep 1.4 GHz WSRT survey (rms noise of 11 μJy/beam) over an area of $\simeq 1.4\,\mathrm{deg}^2$. After correcting for multi-component sources, our sample comprises 1173 objects. Deep multi-band observations are available for 921 (IRAC identified) sources.

Spectroscopic or reliable photometric redshifts are available for 744 of our sources. Using these data we found tight anti-correlations between IRAC band 1 (3.6 μm) or band 2 (4.5 μm) and $\log z$. These were exploited to assign redshifts to the remaining 177 IRAC identified sources. The spread around the mean relations was taken into account using a Monte Carlo approach.

Radio-excess sources, i.e. sources with $\log(L_{1.4\mathrm{GHz}}/\mathrm{SFR})$ above the redshift-dependent threshold defined by Smolčić et al. (2017b), were classified as RL AGNs. The few objects for which no estimate of the SFR was possible were classified on the basis of their radio luminosity, following Magliocchetti et al. (2017). In total, RL AGNs comprise 471 sources ($\simeq$ 40% of the sample).

The other sources were classified as either SFGs or RQ AGNs using the redshift-dependent criterion or the K_s–IRAC diagnostic plot by Messias et al. (2012) or the IRAC colour-colour diagram (Donley et al. 2012), depending on

the available data. We got 310 SFGs and 124 RQ AGNs. Only 16 IRAC identified sources couldn't be classified.

Our classification was checked using the deep X-ray survey with XMM–*Newton* (Brunner et al. 2008) of $\simeq 10\%$ of the field. Three out of the 24 sources ($\sim$13%) in this area classified as SFGs have X-ray luminosity in excess of expectations from star formation, suggesting that they are misclassified RQ AGNs. We have therefore decreased by $\sim$13% the total number of SFGs and correspondingly increased that of RQ AGNs.

We have computed the differential number counts and the luminosity functions at several redshifts of each population and compared them with models and with earlier estimates made using data from different surveys and applying different approaches. A reassuring consistency with both models and other estimates was found, although we find differences in some details.

Our results confirm that RL AGNs dominate the 1.4 GHz counts above $\sim 300\,\mu$Jy, while SFGs+RQ AGNs take over at fainter flux densities.

The deep counts of RQ AGNs and of SFGs have a similar shape, suggesting a similar evolution, consistent with the results by Padovani et al. (2015). At the brightest radio luminosities, SFGs and RQ AGNs have similar space densities at all redshifts, confirming that the evolution is similar. The ratio of RQ AGN to SFG space densities drops rapidly with decreasing radio luminosity. This may be, at least in part, the effect of the difficulty of identifying faint AGNs.

The amplitude of the angular correlation function of our sources is somewhat larger than, but consistent within the errors with that found by Magliocchetti et al. (2017) for a sample of the same depth. On the other hand, the clustering of our RL AGNs is significantly stronger than theirs. We argue that the difference can arise from the different classification criteria. Our results are broadly consistent with clustering properties of radio sources reported by previous studies. We caution however that the comparison requires carefulness because of the different selection frequencies and/or survey depths.

ACKNOWLEDGEMENTS

Thanks are due to the anonymous referee for thoughtful comments that helped improving the paper. We acknowledge support from INAF under PRIN SKA/CTA FORECaST, from the Ministero degli Affari Esteri e della Cooperazione Internazionale - Direzione Generale per la Promozione del Sistema Paese Progetto di Grande Rilevanza ZA18GR02 and the South African Department of Science and Technology's National Research Foundation (DST-NRF Grant Number 113121). Marisa Brienza acknowledges support from the ERC-Stg DRANOEL, no 714245.

DATA AVAILABILITY

The data underlying this article are available in the article and in its online supplementary material.

REFERENCES

Battisti A. J., Calzetti D., Johnson B. D., Elbaz D., 2015, ApJ, 800, 143
Bonaldi A., Bonato M., Galluzzi V., Harrison I., Massardi M., Kay S., De Zotti G., Brown M. L., 2019, MNRAS, 482, 2
Bonato M., et al., 2017, MNRAS, 469, 1912
Bonzini M., Padovani P., Mainieri V., Kellermann K. I., Miller N., Rosati P., Tozzi P., Vattakunnel S., 2013, MNRAS, 436, 3759
Brunner H., Cappelluti N., Hasinger G., Barcons X., Fabian A. C., Mainieri V., Szokoly G., 2008, A&A, 479, 283
Butler A., Huynh M., Kapińska A., Delvecchio I., Smolčić V., Chiappetti L., Koulouridis E., Pierre M., 2019, A&A, 625, A111
Ceraj L., et al., 2018, A&A, 620, A192
Chakraborty A., Dutta P., Datta A., Roy N., 2020, MNRAS, 494, 3392
Condon J. J., 1992, ARA&A, 30, 575
De Zotti G., Massardi M., Negrello M., Wall J., 2010, A&ARv, 18, 1
Donley J. L., et al., 2012, ApJ, 748, 142
Duncan K. J., et al., 2018a, MNRAS, 473, 2655
Duncan K. J., Jarvis M. J., Brown M. J. I., Röttgering H. J. A., 2018b, MNRAS, 477, 5177
Elbaz D., et al., 2010, A&A, 518, L29
Hale C. L., Jarvis M. J., Delvecchio I., Hatfield P. W., Novak M., Smolčić V., Zamorani G., 2018, MNRAS, 474, 4133
Hale C. L., et al., 2019, A&A, 622, A4
Ibar E., Ivison R. J., Best P. N., Coppin K., Pope A., Smail I., Dunlop J. S., 2010, MNRAS, 401, L53
Ivezić Ž., Connolly A., Vanderplas J., Gray A., 2014, Statistics, Data Mining and Machine Learning in Astronomy. Princeton University Press
Landy S. D., Szalay A. S., 1993, ApJ, 412, 64
Lawrence A., et al., 2007, MNRAS, 379, 1599
Lehmer B. D., Alexander D. M., Bauer F. E., Brand t W. N., Goulding A. D., Jenkins L. P., Ptak A., Roberts T. P., 2010, ApJ, 724, 559
Lindsay S. N., et al., 2014, MNRAS, 440, 1527
Lockman F. J., Jahoda K., McCammon D., 1986, ApJ, 302, 432
Lonsdale C. J., et al., 2003, PASP, 115, 897
Magliocchetti M., Popesso P., Brusa M., Salvato M., Laigle C., McCracken H. J., Ilbert O., 2017, MNRAS, 464, 3271
Małek K., et al., 2018, A&A, 620, A50
Mancuso C., et al., 2017, ApJ, 842, 95
Mauduit J. C., et al., 2012, PASP, 124, 714
Messias H., Afonso J., Salvato M., Mobasher B., Hopkins A. M., 2012, ApJ, 754, 120
Novak M., et al., 2017, A&A, 602, A5
Ocran E. F., Taylor A. R., Vaccari M., Green D. A., 2017, MNRAS, 468, 1156
Ocran E. F., Taylor A. R., Vaccari M., Ishwara-Chand ra C. H., Prandoni I., 2020a, MNRAS, 491, 1127
Ocran E. F., Taylor A. R., Vaccari M., Ishwara-Chand ra C. H., Prandoni I., Prescott M., Mancuso C., 2020b, MNRAS, 491, 5911
Orenstein B. J., Collier J. D., Norris R. P., 2019, MNRAS, 484, 1021
Padovani P., 2016, A&ARv, 24, 13
Padovani P., Bonzini M., Kellermann K. I., Miller N., Mainieri V., Tozzi P., 2015, MNRAS, 452, 1263
Peebles P. J. E., 1980, The large-scale structure of the universe. Princeton University Press
Planck Collaboration 2015, preprint, (arXiv:1502.01589)
Prandoni I., Guglielmino G., Morganti R., Vaccari M., Maini A., Röttgering H. J. A., Jarvis M. J., Garrett M. A., 2018, MNRAS, 481, 4548

Rana S., Bagla J. S., 2019, MNRAS, 485, 5891
Ranalli P., Comastri A., Setti G., 2003, A&A, 399, 39
Schmidt M., 1968, ApJ, 151, 393
Shirley R., et al., 2019, MNRAS, 490, 634
Smolčić V., et al., 2017a, A&A, 602, A1
Smolčić V., et al., 2017b, A&A, 602, A2
Smolčić V., et al., 2017c, A&A, 602, A6
Vaccari M., 2015, in Proceedings of "The many facets of extragalactic radio surveys: towards new scientific challenges" (EXTRA-RADSUR2015). 20-23 October 2015. Bologna. p. 27 (arXiv:1604.02353)
Vaccari M., 2016, in Napolitano N. R., Longo G., Marconi M., Paolillo M., Iodice E., eds, Vol. 42, The Universe of Digital Sky Surveys. p. 71 (arXiv:1508.06444), doi:10.1007/978-3-319-19330-4˙10
Vanderplas J., Connolly A., Ivezić Ž., Gray A., 2012, in Conference on Intelligent Data Understanding (CIDU). pp 47 –54, doi:10.1109/CIDU.2012.6382200
Wilman R. J., et al., 2008, MNRAS, 388, 1335

This paper has been typeset from a TEX/LATEX file prepared by the author.